processes

Article

Centrifugal Pump Cavitation Fault Diagnosis Based on Feature-Level Multi-Source Information Fusion

Mengbin Song [1], Yifan Zhi [2], Mengdong An [3], Wei Xu [4], Guohui Li [5] and Xiuli Wang [3,*]

1 LEO Group Hunan Pump Co., Ltd., Jiuhua Demonstration Zone, Xiangtan 411201, China; songmb@leogroup.cn
2 China Nuclear Power Engineering Co., Ltd., Beijing 100840, China; zhiyf@cnpe.cc
3 Research Center of Fluid Machinery Engineering and Technology, Zhenjiang 212013, China; amdujs@163.com
4 School of Energy and Power Engineering, Jiangsu University, Zhenjiang 212013, China; xuwei791837@hotmail.com
5 GongQing Institute of Science and Technology, Jiujiang 332020, China; lghgqkj@163.com
* Correspondence: ujslthb@163.com

Abstract: In nuclear power systems, centrifugal pumps often need to operate under extreme conditions. However, accurately determining the cavitation status of centrifugal pumps under such extreme conditions is challenging. To improve the recognition accuracy of the three statuses of non-cavitation, incipient cavitation, and severe cavitation while improving the anti-interference capability of the monitoring system, this study extracted cavitation features from centrifugal pumps' motor current and vibration signals under three different operational conditions. It fused the features using feature-level multi-source information fusion (MSIF) based on the backpropagation neural network (BPNN) or support vector machine (SVM) to construct a cavitation status recognition model and analyzed the results to compare with those of recognition without information fusion. The results show that, compared with one signal source, MSIF can significantly improve the recognition accuracy of cavitation statuses. Combined current and pump casing axial monitoring based on the BPNN is the optimal scheme, with an overall recognition accuracy of 97.3% for all operational conditions, compared to 73.9% for the single current signal and 89.3% for the single casing axial vibration signal. These research results can guide the monitoring of cavitation statuses in practical engineering, as well as timely intervention at incipient cavitations to reduce structural damage to centrifugal pumps and prolong service life.

Keywords: centrifugal pump; cavitation; feature-level multi-source information fusion; backpropagation neural network; support vector machine

Citation: Song, M.; Zhi, Y.; An, M.; Xu, W.; Li, G.; Wang, X. Centrifugal Pump Cavitation Fault Diagnosis Based on Feature-Level Multi-Source Information Fusion. *Processes* **2024**, *12*, 196. https://doi.org/10.3390/pr12010196

Academic Editors: Blaž Likozar and Wei Sun

Received: 6 October 2023
Revised: 4 January 2024
Accepted: 11 January 2024
Published: 16 January 2024

1. Introduction

Centrifugal pumps are fluid machines commonly used in nuclear power systems, often required to operate continuously under extreme conditions, such as high temperatures, high pressures, high humidity, or the transport of hazardous media. Cavitation is a typical centrifugal pump failure; it not only affects the velocity and pressure distribution in the pipe, but also causes vibration and noise due to the shock load generated by the collapse of the bubbles, which will damage the impeller and other flow components, reducing the efficiency, stability, safety, and concealment of the centrifugal pump [1,2]. Monitoring cavitation in centrifugal pumps is vital for ensuring the long-term stable operation of nuclear power systems. Traditional cavitation monitoring in centrifugal pumps involves using invasive sensors to measure flow and pressure for calculating the head, with a 3% decrease in head serving as an indicator of cavitation occurrence [3]. Invasive sensors destroy the pipe's structural integrity, leading to a deterioration in the stability of the centrifugal pump under long-term operational conditions, and the reliability of the data

collected by the sensor is reduced [4]. Especially in extreme conditions, achieving the accurate monitoring of cavitation statuses is more complicated.

Current research on cavitation fault diagnosis in centrifugal pumps primarily focuses on employing non-invasive sensors to monitor variations in signals, such as motor current, vibrations, and noise, induced during the cavitation process to monitor cavitation statuses indirectly [5,6]. These methods enable cavitation monitoring and the predictive maintenance of centrifugal pumps without modifying the pipe structure or operational conditions. They offer the advantages of improved productivity, ease of operation, and cost-effectiveness, making them widely applicable in various extreme operational conditions. However, under extreme operating conditions, the monitoring system's interference resistance should be prioritized, as noise signals are highly susceptible to interference from other industrial equipment, which limits this method's practical use [7]. Vibration signals are the most commonly applied method. Razieh et al. [8] employed discrete wavelet transform (DWT) and empirical mode decomposition (EMD) to extract the cavitation features from vibration signals and constructed a recognition model for three cavitation statuses. Hui Sun et al. [9] employed a time–frequency signal analysis method based on cyclostationary theory to extract frequency characteristic components from non-stationary vibration signals under cavitation and sealing damage conditions. This approach aims to enhance the efficiency and reliability of the pump. While vibration signals are highly sensitive to cavitation, their accuracy is directly affected by the measurement location [10], and the signal acquisition process is prone to environmental interference [11]. Methods for monitoring cavitation statuses using motor current signals have emerged in recent years. Kipervasser et al. [12] investigated the influence of cavitation and the extent of its development on the mechanical power consumption of an electric motor. They established a joint mathematical model for the centrifugal pump and synchronous motor, leading to conclusions regarding the likelihood of cavitation based on recorded motor currents. Hui Sun et al. [6] demonstrated that the root mean square (RMS) values of the current signal components are sensitive to incipient cavitation by using the Hilbert–Huang transform (HHT) method to extract the cavitation features. This method has the advantages of being simple, feasible, affordable, and remotely monitored in real time [13]. Compared to vibration signals, current signals contain less noise [14] and are more resistant to interference, but there are relatively few studies on cavitation status recognition based on motor current signals.

In fault diagnosis for rotating machinery, the most common approach is to use one type of sensor for signal acquisition. However, the structure of centrifugal pumps is complex, and the operating environment often has random factors. Relying solely on one type of signal source can pose challenges in ensuring the accuracy and completeness of the acquired information and in providing immunity to interference [15]. MSIF is an emerging interdisciplinary field with significant development in recent years; it combines redundant or complementary information from one or multiple sensors, achieving cross-validation and mutual data compensation, which can enhance the performance of information systems, extract more valuable information, and strengthen system resilience and stability [16]. L. Dong et al. [17] proposed a multi-measurement point cavitation feature signal fusion model based on vibration signals, and the accuracy of this method for recognizing cavitation status is still over 90%, even when one of the measurement points is highly disturbed. Huaqing Wang et al. [18] proposed a rotating machinery fault recognition method based on the fusion of multiple vibration signals and an optimized bottleneck layer convolutional neural network (MB-CNN). This method integrates information to obtain richer features than a single vibration signal, enhancing recognition accuracy and achieving faster convergence speeds.

Although MSIF has been applied to recognize the cavitation status of centrifugal pumps, most cases rely on a single type of sensor. Joint diagnosis using different sensor types is relatively uncommon. In order to improve the accuracy and interference resilience of the cavitation monitoring system, this study utilized current and vibration sensors to collect signals from different cavitation statuses in centrifugal pumps. These

signals undergo different levels of filtering and decomposition to extract cavitation features, followed by classification training using a BPNN and SVM to recognize the cavitation status. Subsequently, a novel cavitation status recognition model was established based on feature-level MSIF. The optimal joint cavitation diagnosis approach employing current and vibration sensors is determined by comparing and analyzing the recognition results with those from a single signal source. The research findings have a certain reference value for the engineering application of centrifugal pump cavitation diagnosis. Also, it provides a basis for the joint diagnosis of centrifugal pump cavitation status using multiple types of sensors.

2. Research Methodology

2.1. Test System of Cavitation in the Centrifugal Pump

For this test, a single-stage, single-suction centrifugal pump was the test pump; its specific speed was n_s = 62, head H = 10 m, rated flow rate Q_d = 13 m^3/h, and rotational speed n = 1450 r/min. In order to photograph the bubbles around the impeller conveniently, the impeller and pump casing used transparent Plexiglas. The test system is shown in Figure 1. Data acquisition for this test included the flow rate, inlet and outlet pressure, motor current and voltage, rotational speed, and vibration signals. The data acquisition system consisted of graphical user interfaces (GUIs) based on MATLAB R2022a and a National Instruments (NI) capture card based on LabVIEW. The GUI collected the flow rate, inlet and outlet pressure, motor current, and voltage signals. NI collected the vibration signals and rotational speed. Figure 2 shows the sensors used in this test. The head (H) was calculated using pressure and flow sensors. The current signal was acquired using a Hall sensor for one of the three-phase asynchronous motor phases with a frequency of 1 kHz. The vibration signals were collected by acceleration sensors at four measurement points, labelled as A, B, C, and D in Figure 1, with a frequency of 10 kHz.

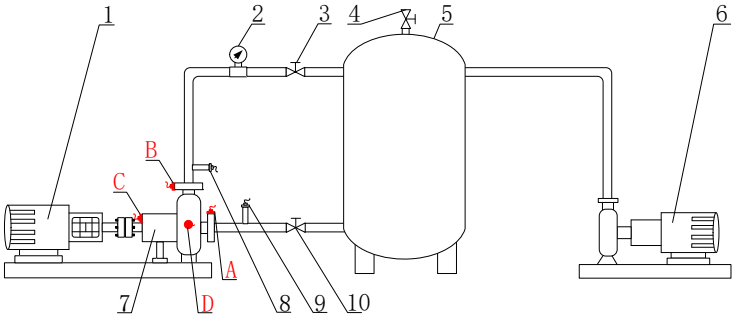

Figure 1. Schematic diagram of the test system: 1—motor; 2—flow meter; 3—outlet valve; 4—venting valve; 5—pressure stabilizing tank (water tank); 6—vacuum pump; 7—test centrifugal pump; 8—outlet pressure sensor; 9—inlet pressure sensor; 10—inlet valve. Vibration sensor location: A—inlet; B—outlet; C—pump casing axial; D—pump casing radial.

(**a**) (**b**) (**c**)

Figure 2. Sensors used in the test: (**a**) pressure sensor; (**b**) Hall current sensor; (**c**) acceleration sensor.

After adjusting the outlet valve, cavitation tests were performed at three flow conditions: 0.75 Q_d, 1.0 Q_d, and 1.25 Q_d. The cavitation performance curves of the test pump were plotted for three flow rates. The critical cavitation point at each flow rate was determined based on a 3% head loss criterion [3]. Two important parameters, the cavitation number (σ) and head coefficient (Ψ), are calculated as follows:

$$\Psi = \frac{H}{u_0^2/2g} \tag{1}$$

$$\sigma = \frac{P - P_v}{0.5\rho u_0^2} \tag{2}$$

where u_0 is the flow rate (m^3/s); g is gravity acceleration; and P is the inlet static pressure (Pa). The medium used in the test is water; its density (ρ) is 998 kg/m^3, and the saturated vapor pressure (P_v) of water at ambient temperature (20 °C) is 2.34 kPa.

2.2. Uncertainty Analysis

A test uncertainty analysis was employed to validate the accuracy of the test results. The comprehensive uncertainty of a test comprises two parts: system uncertainty (E_S) and random uncertainty (E_r). The test method, equipment design parameters, and accuracy primarily influence system uncertainty, E_S. Random uncertainty (E_r) mainly arises from random errors and external environmental disturbances [19].

E_S is given in the following formula:

$$E_S = \pm\sqrt{\left(\frac{f_m}{k}\right)^2 + \left(\frac{f_c}{k}\right)^2} \tag{3}$$

where f_m is the uncertainty of the sensor, f_c is the system uncertainty of the acquisition instrument, and the coverage factor (k) is 1.96 [19]. The system uncertainty for each measurement parameter is shown in Table 1.

Table 1. The system uncertainty (%) of each measurement parameter.

	Head	Flow Rate	Pressure	Rotational Speed	Vibration	Current
f_m	±0.15	±0.12	±0.20	±0.20	±0.50	±0.20
f_c	±0.10	±0.10	±0.15	±0.15	±0.10	±0.10
E_S	±0.0920	±0.0797	±0.1276	±0.1276	±0.2254	±0.0989

E_r is given in the following formula:

$$E_r = \pm\frac{t_{n-1}S_x}{\overline{x}\sqrt{n}} \times 100\% \tag{4}$$

$$Sx = \sqrt{\frac{1}{n-1}\sum_{i=1}^{n}(x_i - \overline{x})^2} \tag{5}$$

where S_x is the standard deviation, x_i is the measured data, $\overline{x}$ is the arithmetic mean of the data, t_{n-1} is the confidence coefficient, and n is 10; thus, t_{n-1} = 2.262 (α = 95%). The test data were collected at different time points under rated operating conditions to calculate the random uncertainty of the test, as shown in Table 2.

Table 2. The test data were collected at different time points under rated operating conditions.

	Head	Flow Rate	Pressure	Rotational Speed	Vibration	Current
1	8.46	13.01	91.16	1450	0.1142	4.92
2	8.47	13.00	91.14	1450.5	0.1149	4.92
3	8.46	13.07	91.20	1450	0.1134	4.93
4	8.47	12.93	91.07	1451.5	0.1053	4.91
5	8.46	13.03	91.18	1450	0.1095	4.91
6	8.47	13.10	91.29	1451	0.1154	4.92
7	8.45	12.92	91.06	1450	0.1147	4.93
8	8.44	13.05	91.21	1450	0.1292	4.93
9	8.46	13.10	91.28	1451	0.1136	4.93
10	8.42	13.08	91.24	1450	0.1152	4.94
$\overline{x}$	8.456	13.029	91.183	1450.4	0.1148	4.924
S_x	0.0158	0.0647	0.0785	0.5676	0.0065	0.0097

The random uncertainty of each measurement parameter in Table 2 was calculated based on its mean and standard deviation, respectively, and the results are shown in Table 3.

Table 3. Random uncertainty (%) of each measurement parameter.

	Head	Flow Rate	Pressure	Rotational Speed	Vibration	Current
E_r	±0.1335	±0.3553	±0.0616	±0.0280	±3.7777	±0.1403

The comprehensive uncertainty € was calculated by combining the system uncertainty (E_S) and the random uncertainty (E_r) of each measurement parameter using the following formula:

$$E = \pm\sqrt{E_r^2 + E_S^2} \tag{6}$$

The comprehensive uncertainty of each measurement parameter is shown in Table 4. The comprehensive uncertainty for signals other than vibration is relatively low, resulting in high data reliability. Vibration signals exhibit a higher comprehensive uncertainty of approximately ±3.78%, primarily due to random uncertainty, indicating that the reliability of vibration signal data is not high. The Table 2 data reveal that, under identical operational conditions, only the vibration signals displayed significant fluctuations. This phenomenon may be attributed to external vibrations and noises in the testing environment, adversely impacting the stable acquisition.

Table 4. Comprehensive uncertainty (%) of each measurement parameter.

	Head	Flow Rate	Pressure	Rotational Speed	Vibration	Current
E_S	±0.092	±0.0797	±0.1276	±0.1276	±0.2254	±0.0989
E_r	±0.1156	±0.3078	±0.0533	±0.0243	±3.7777	±0.1216
E	±0.1478	±0.318	±0.1383	±0.1298	±3.7844	±0.1717

2.3. Signal Pre-Processing and Feature Extraction

2.3.1. Motor Current Signal Pre-Processing and Feature Extraction

In order to enhance the signal-to-noise ratio of the current signal, it is crucial to filter out the 50 Hz industrial frequency component. Singular value decomposition (SVD) can effectively eliminate strong interference signals while preserving weaker ones, making it an appropriate pre-processing technique for the current signal [20].

Based on the SVD pre-processing, empirical mode decomposition (EMD) and variational mode decomposition (VMD) were subsequently employed to extract the cavitation features. EMD decomposes a signal based on its intrinsic time scale characteristics without any pre-set basis function. EMD decomposed the current signal into seven intrinsic mode functions (IMFs), each preserving local feature information at different time scales of the

original signal [21]. VMD is an adaptive and entirely non-recursive signal processing method. It addresses issues commonly encountered in EMD, such as endpoint effects and mode component mixing. VMD can decompose signals into multiple relatively stationary components, each containing different frequency scales, known as bandwidth-limited intrinsic mode functions (BIMFs). This method is well-suited for analyzing non-stationary time series [22]. VMD has several essential parameters: the decomposition level (K), the penalty factor (α), the fidelity coefficient (τ), and the convergence threshold (ε). The value (over-binning or under-binning) of K directly impacts the filtering effect; it was determined to be 7 using the central frequency method. As α increases, the decay on both sides of the central frequency becomes faster, and a well-adapted value of 2000 was chosen. The fidelity coefficient (τ) was set to 0.3, which can ensure the integrity of the signal after reconstruction. The convergence threshold (ε) is typically set to 1×10^{-5}, but was adjusted to 1×10^{-7} [23].

After selecting the modal decomposition from EMD and VMD that is more suitable for processing the current signal, the energy proportion (e_i), variance (s_i), kurtosis (k_i), skewness (γ_i), and RMS value (η_i) of each component were calculated as the eigen-matrix (T_1) of the current cavitation status recognition; see Equation (7). The value of e_i represents signal intensity; s_i quantifies data dispersion; k_i characterizes data distribution properties, with $k_i \approx 3$ indicating a close approximation to a normal distribution, while values significantly different from 3 indicate higher skewness or dispersion; γ_i describes the symmetry of the data value distribution, with larger absolute values of γ_i indicating a greater degree of skewness in the distribution; and η_i represents the effective value of energy.

$$T_1 = \begin{bmatrix} e_1 & e_2 & e_3 & \cdots & e_i \\ s_1 & s_2 & s_3 & \cdots & s_i \\ \mathrm{k}_1 & k_2 & k_3 & \cdots & k_i \\ \gamma_1 & \gamma_2 & \gamma_3 & \cdots & \gamma_\mathrm{i} \\ \eta_1 & \eta_2 & \eta_3 & \cdots & \eta_\mathrm{i} \end{bmatrix} \tag{7}$$

2.3.2. Vibration Signal Pre-Processing and Feature Extraction

Vibration signal acquisition is often accompanied by noise from the external environment and the test instrument itself. Consequently, signal pre-processing for noise reduction becomes essential. Wavelet domain denoising has proven effective in preserving signal spikes and local highlights [24]. Therefore, the db4 wavelet was employed to decompose the vibration signal with a decomposition level of 3, and the thresholding process utilized soft threshold shrinkage.

After the noise reduction of the vibration signals, five time-domain dimensionless characterization quantities (Q_t), including the mean, variance, crag, skewness, and RMS, were calculated for the vibration data under each operational condition, constituted the eigen-matrix (T_2) for vibration cavitation status recognition, which is similar to Equation (7).

2.4. Cavitation Status Recognition

2.4.1. Cavitation Status Recognition Model Based on BPNN

The BPNN, a multi-layer feed-forward neural network, is trained using the error backpropagation algorithm. The fundamental concept involves inputting training samples and iteratively adjusting the network's weights and thresholds through backpropagation to minimize the sum of squared errors in the output layer, thereby aligning the network's output with the target [25].

In practical engineering applications, the accurate monitoring of incipient cavitation is crucial. It allows for timely intervention and maintenance when cavitation initiates, reducing structural damage to centrifugal pumps and extending their operational lifespan. Therefore, all recognition models in this study categorized cavitation statuses into three classifications: non-cavitation, incipient cavitation, and severe cavitation, denoted as Y_1, Y_2, and Y_3, respectively. From the previous section, the current signal was modally decomposed into seven components, and each component has five eigenvectors, so the number of sample

features is 5 × 7. The BPNN hidden layer contained 40 nodes, and training was conducted over 1000 iterations with a learning rate of 0.02. The vibration signal features comprised five eigenvectors. The neural network employed 14 hidden-layer nodes, and training consisted of 800 iterations with a learning rate of 0.03. Each training model utilized 75% of the samples as the training set and 25% as the test set. The model's training was based on MATLAB R2022a pattern recognition, and the confusion matrixes and ROC curves evaluated the training results.

2.4.2. Cavitation Status Recognition Model Based on SVM

In order to analyze the classification performance of different cavitation identification models comparatively, the support vector machine (SVM) was concurrently utilized to conduct classification training on cavitation features. The standard SVM is designed for binary classification problems and cannot directly handle multi-classification problems. A one-against-all SVM was employed [26]; by modifying the optimization problem of the standard SVM, it is possible to achieve a single iteration for computing three decision boundaries in cavitation identification. The classification criteria for cavitation states follow the three classifications mentioned earlier.

The penalty parameter (C), the kernel function, and the selection of related parameters significantly impact the SVM effect [27]. The Gaussian radial basis function (RBF) was chosen as the kernel function for the SVM and employed particle swarm optimization (PSO) to optimize the penalty factor (C) and the RBF self-contained function (g), resulting in the optimal combination of (C, g) [28]. Again, 75% of the samples were taken as training and 25% as test sets. For current signals, the model achieved a fitness of 93.7% after sample training, with the optimal (C, g) combination being (10.0929, 6.3211). The model converged in approximately ten iterations, demonstrating a relatively rapid convergence rate. Similarly, for vibration signals, utilizing the same SVM model resulted in a fitness of 97.7% after training, with the optimal (C, g) combination being (12.0929, 5.3211). The model converged in approximately eight iterations, indicating a relatively fast convergence rate.

2.5. Multi-Source Information Fusion

The system structure of feature-level MSIF based on a BPNN or SVM is shown in Figure 3. After extracting features from the original data, the feature data are standardized according to specific rules to obtain consistent types of feature vectors. These vectors are then input into the BPNN or SVM to obtain classification decisions [29–31].

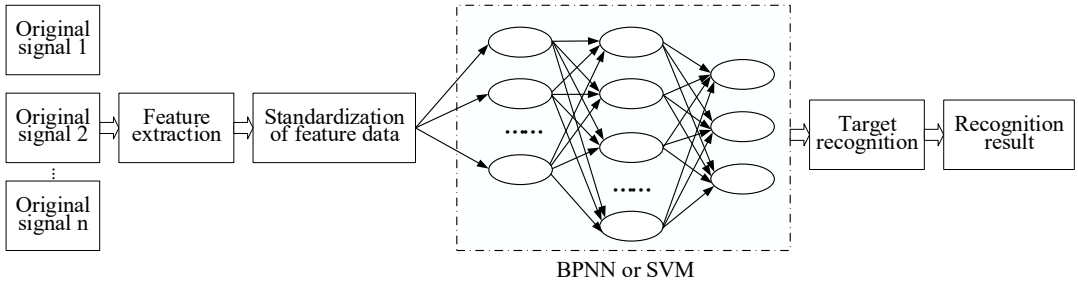

Figure 3. Structure of feature-level MSIF based on BPNN or SVM.

Before performing information fusion, it was necessary to standardize T_1 and T_2. The method chosen was linear function normalization (min–max scaling), which was applied to normalize all row vectors of T_1 and T_2, except for kurtosis, k_i. This study performed feature-level fusion on all vibration measurement point signals, current-inlet vibration signals, current-outlet vibration signals, current-casing axial vibration signals, and current-casing radial vibration signals for cavitation status recognition. Cavitation recognition employed the same BPNN and SVM three-classification models, utilizing 75% of the samples as a training set and 25% as a testing set. For the BPNN model, 50 hidden layers were used, with training conducted for 1200 iterations and the learning rate set to 0.02.

3. Results and Analysis

3.1. Cavitation Performance Test Results and Analysis

The cavitation performance curves of the centrifugal pump are shown in Figure 4, which reveals that the head coefficient (Ψ) initially remains relatively constant, then it starts to decrease with the decrease in the cavitation number (σ), and the cavitation occurs earlier under the large flow rate. Based on the 3% reduction in the head criterion [3], the cavitation inception numbers (σ_H) under various conditions were determined as follows: σ_H = 0.308 at 0.75 Q_d, σ_H = 0.359 at 1.0 Q_d, and σ_H = 0.386 at 1.25 Q_d. The black dashed line in the figure indicates the σ_H for each condition.

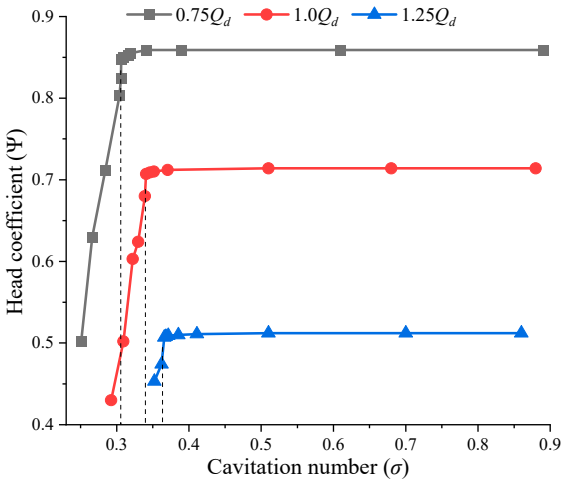

Figure 4. Cavitation performance curves.

The inception cavitation status of the test pump under different operational conditions is depicted in Figure 5; it is evident that, during inception cavitation, there are relatively few bubbles within the impeller. These bubbles are primarily concentrated near the suction side of the impeller's leading edge. As the fluid continues to flow, the bubbles gradually collapse and disappear near the middle of the impeller.

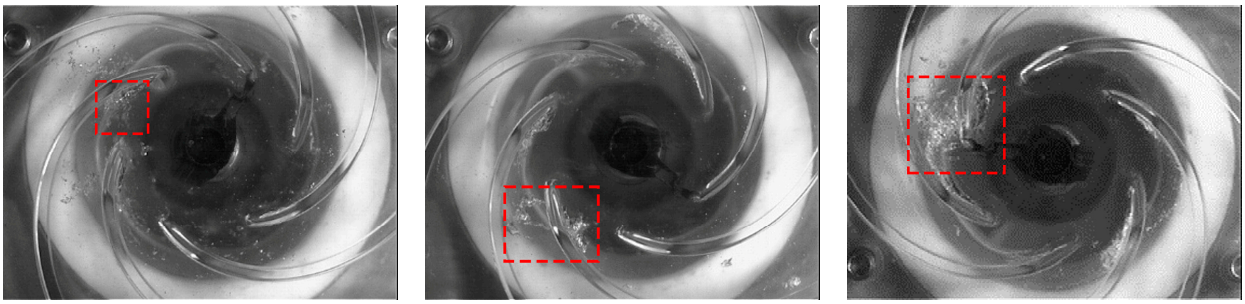

(**a**) (**b**) (**c**)

Figure 5. Images of incipient cavitation under different operational conditions: (**a**) 0.75 Q_d, σ = 0.308; (**b**) 1.0 Q_d, σ = 0.359; (**c**) 1.25 Q_d, σ = 0.386. (Red dotted line marks the location of the obvious aggregation of bubbles).

Combining the cavitation performance curves and high-speed photography results, the cavitation statuses under each operational condition were triple classified using the cavitation number (σ). The classification results are shown in Table 5.

Table 5. The cavitation number threshold of each cavitation status under different operational conditions.

	0.75 Q_d	**1.0 Q_d**	**1.25 Q_d**
Y_1	$\sigma > 0.308$	$\sigma > 0.359$	$\sigma > 0.386$
Y_2	$0.308 > \sigma > 0.288$	$0.358 > \sigma > 0.304$	$0.386 > \sigma > 0.336$
Y_3	$\sigma < 0.259$	$\sigma < 0.279$	$\sigma < 0.298$

3.2. Motor Current Signal Pre-Processing and Feature Extraction Results and Analysis

The raw current signal within 0.4 s at 1.0 Q_d was analyzed. Its power spectral density (PSD) is shown in Figure 6. The 50 Hz industrial frequency and its significant harmonics primarily dominate the current signal. These harmonics include the 250 Hz and 350 Hz modulation signals derived from the 300 Hz blade and the 50 Hz industrial frequencies. Moreover, the 50 Hz industrial frequency signal constitutes a substantial portion of the current signal, making it prone to submerge small signals containing cavitation features. Figure 7 shows the SVD filtered results of the current signal at 1.0 Q_d for various cavitation numbers. It is observed that the mains frequency signal is effectively removed. As the cavitation number decreases, there is a slight increase in the bandwidth and amplitude of the frequency bands on both sides of 50 Hz in the frequency domain, as shown in Figure 8. This is primarily due to the increasing irregular motion of the fluid on the impeller caused by intensified cavitation, resulting in a greater torque exerted directly on the impeller, which is reflected in the current signal; it indicates that the pre-processing of removing the mains frequency signal with SVD is effective, but SVD cannot effectively extract the small signals that characterize cavitation features. Therefore, additional signal analysis methods are needed for further processing.

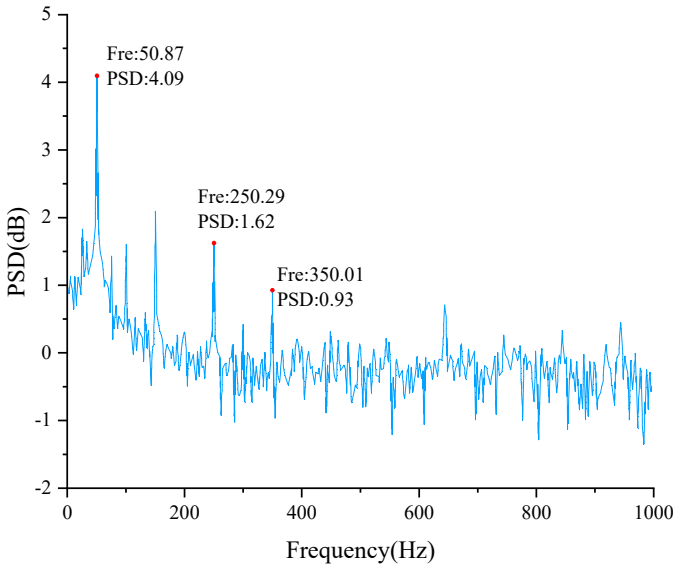

Figure 6. The PSD diagram of the raw current signal.

After further processing with EMD and VMD following SVD, Figure 9 displays the time-domain and frequency-domain plots of the first five current signal components at 1.0 Qd. From Figure 9a, it can be observed that IMF1 primarily contains high-frequency signals, IMF2 mainly contains signals ranging from 500 Hz to 2000 Hz, and IMF3 predominantly contains signals below 1000 Hz. However, each component exhibits modal mixing. In contrast, the five BIMF components obtained from VMD exhibit distinct central frequencies that increase sequentially, showing no modal mixing and a higher degree of modal separation.

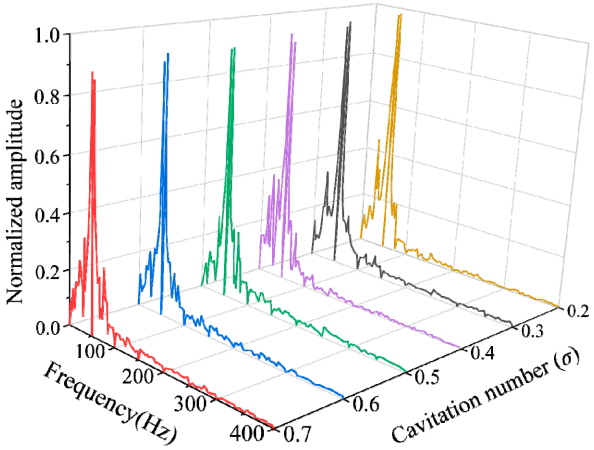

Figure 7. Results of the current signal after SVD processing under different cavitation numbers.

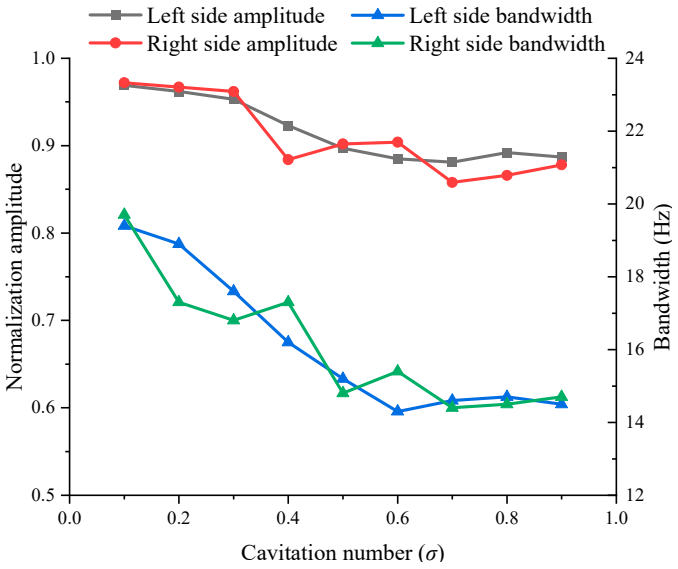

Figure 8. Frequency band amplitude and bandwidth variation curves.

In order to distinguish the cavitation status under different operational conditions, the RMS values of the components obtained from VMD were calculated for analysis. Taking the RMS values of BIMF1 as an example, as shown in Figure 10, BIMF1-RMS exhibits significant variation, as the cavitation number decreases at 1.25 Q_d, with a reference RMS value of 0.0955 for non-cavitation. At 1.0 Q_d and 0.75 Q_d, the variation in BIMF1-RMS during the cavitation stage is less pronounced than that at 1.25 Q_d, which also shows an increase. The reference RMS values for non-cavitation are 0.0933 and 0.0912, respectively. This phenomenon arises because BIMF1's central frequency is in the vicinity of the rotational frequency's sideband spectrum. During cavitation in the centrifugal pump, the impact of the fluid on the impeller increases, affecting the rotational frequency, which leads to a reduction in the energy of the rotational frequency in the current signal and an enhancement in the sideband frequency spectrum near the rotational frequency. Under high-flow conditions, cavitation is more likely to occur, and severe cavitation leads to turbulence. At this point, the impact of the fluid on the impeller is most significant, and a higher level of harmonic energy is injected. Therefore, BIMF1-RMS, obtained through the SVD-VMD decomposition of the current signal, can partially characterize the cavitation status. Furthermore, as the flow rate increases, this cavitation characteristic becomes clearer.

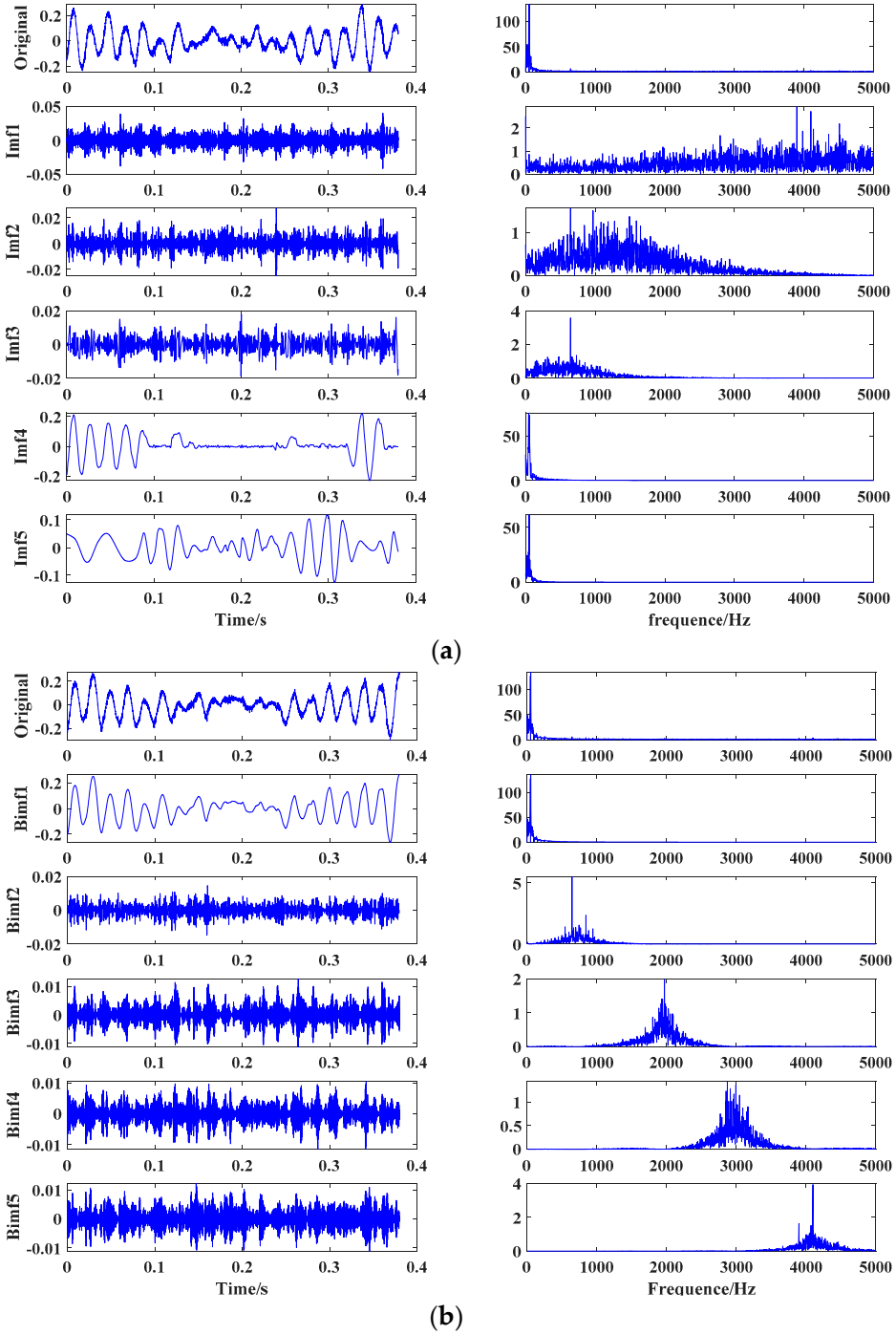

Figure 9. The results of the current signal processed by SVD-EMD and SVD-VMD at 1.0 Q_d: (**a**) SVD-EMD; (**b**) SVD-VMD.

Taking BIMF1-RMS at 1.0 Q_d as an example, according to the cavitation number thresholds in Table 5, the characteristic values for BIMF1-RMS in non-cavitation, incipient cavitation, and severe cavitation were determined to be 0.0933, 0.0934, and 0.0932, respectively. Similar processing was applied to the energy percentage, variance, kurtosis, and skewness of BIMF1, yielding various feature data for this component, as shown in Table 6. The same method was employed to process the respective VMD components for the other two operational conditions and completed the cavitation feature extraction from the current signal.

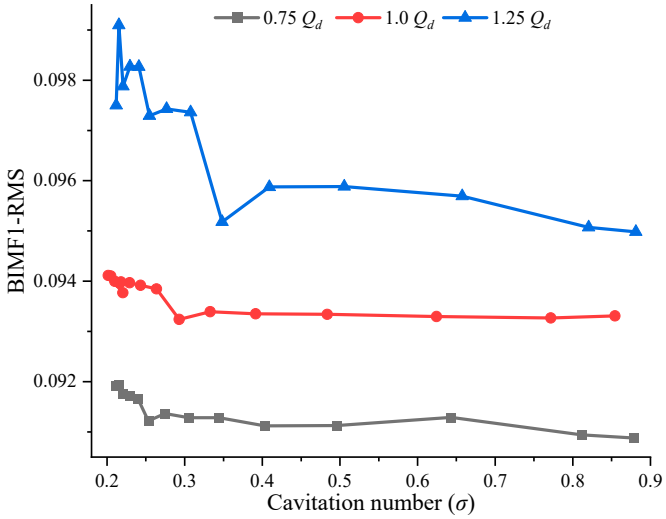

Figure 10. Plot of BIMF1 component RMS values at each cavitation stage.

Table 6. The cavitation features of BIMF1.

Cavitation Status	Energy Percentage	Variance	Kurtosis	Skewness	RMS	Sample Size
Y_1	0.8946	0.0094	2.9392	−0.1274	0.0933	130
Y_2	0.8925	0.0101	2.7794	−0.1198	0.0934	175
Y_3	0.8916	0.0091	2.8061	−0.1923	0.0932	195

3.3. Vibration Signal Pre-Processing and Feature Extraction Results and Analysis

Taking the axial casing vibration signal collected within 0.1 s at 1.0 Q_d as an example, a comparative analysis before and after filtering was conducted, and the results are depicted in Figure 11. After wavelet domain denoising, most tiny components in the original vibration signal were successfully eliminated. The filtered signal preserves the effective values from the raw data and exhibits a smoother profile, with the retained energy components accounting for 74.98%.

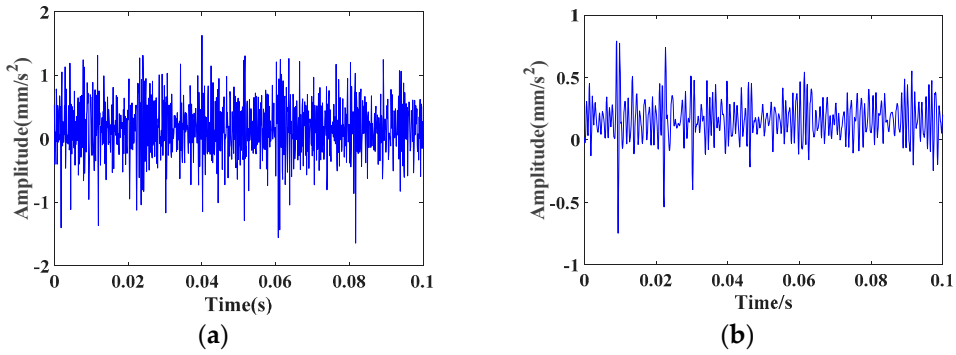

Figure 11. Comparison of vibration signal before and after wavelet domain denoising: (**a**) original vibration signal; (**b**) filtered vibration signal.

The time-domain plots of vibration signals from the same measurement point under different cavitation statuses exhibit clear distinctions. Taking the example of the casing axial measurement point at 1.0 Q_d within 1.0 s, the time-domain plot after pre-processing with wavelet denoising is shown in Figure 12. The figure shows that the amplitude range of vibration acceleration gradually increases as the cavitation number decreases. This observation indicates that with the intensification of cavitation, the collapse of bubbles leads to increased casing vibration.

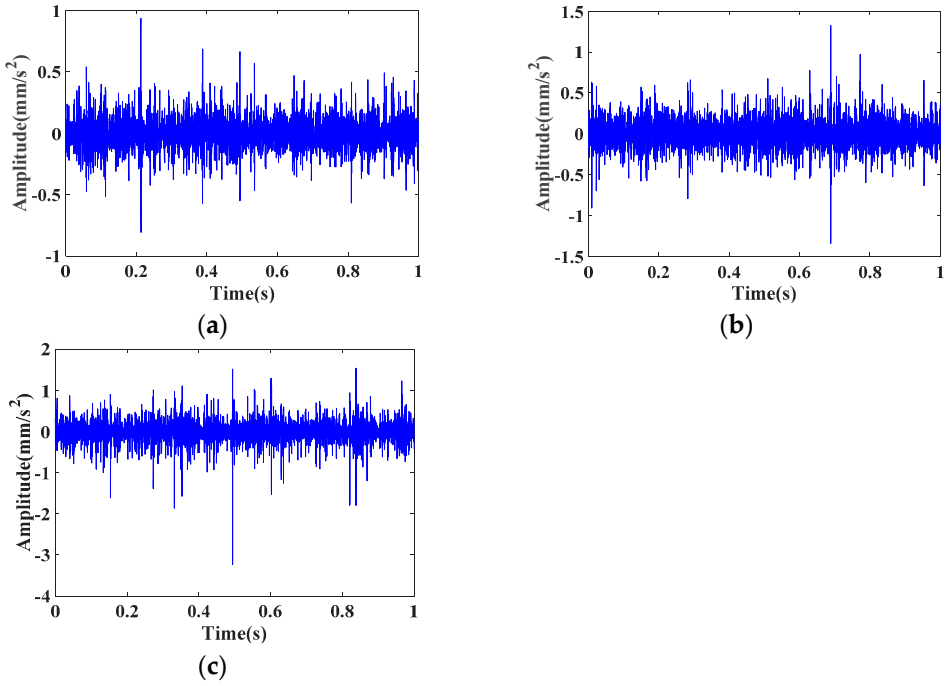

Figure 12. The casing axial vibration signals in different cavitation statuses at 1.0 Q_d: (**a**) σ = 0.359; (**b**) σ = 0.304; (**c**) σ = 0.279.

Taking the five time-domain dimensionless characterization quantities of casing axial vibration signals at 1.0 Q_d as an example, as shown in Figure 13, it is evident that various characteristics of the casing axial under different cavitation statuses, except for the average, exhibit significant differences. Among these characteristics, the kurtosis, RMS, and variance show a clear increasing trend with intensified cavitation, with kurtosis exhibiting the most significant increase and consistently exceeding three. Skewness displays a noticeable decreasing trend and remains below 0, indicating a distinct left (negative) skewness trend in the vibration signal with increased cavitation. It can be concluded that the vibration signal at the casing axial measurement point provides significant discrimination among different cavitation statuses.

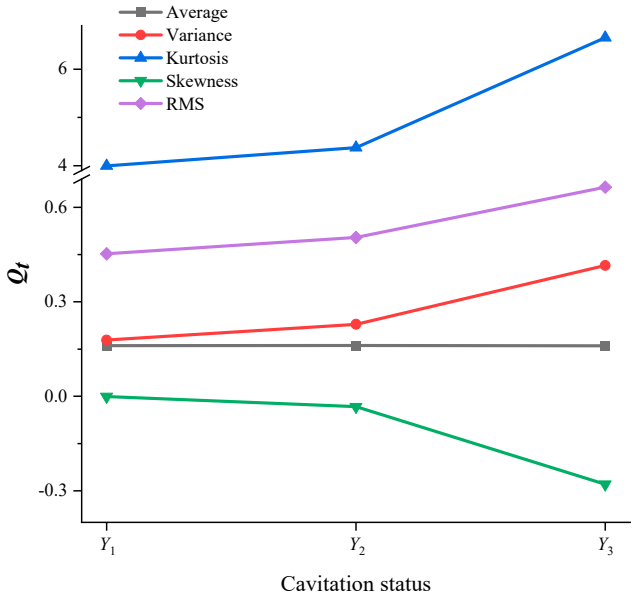

Figure 13. Five time-domain dimensionless characterizations of casing axial vibration signals at 1.0 Q_d.

Based on the cavitation number thresholds provided in Table 5, the cavitation features of each vibration measurement point under 1.0 Q_d were extracted, as shown in Table 7. The same method was applied to process the data from the other two operational conditions to complete the extraction of cavitation features from the vibration signals.

Table 7. The cavitation features of each vibration measuring point under 1.0 Q_d.

Measurement Point	Average	Variance	Kurtosis	Skewness	RMS	Sample Size	Cavitation Status
Inlet	0.1512	0.0123	3.2297	−0.0118	0.1876	140	Y_1
	0.1513	0.0141	3.1506	0.0183	0.1926	229	Y_2
	0.1522	0.0151	3.1709	−0.0478	0.1957	131	Y_3
Outlet	0.1494	0.0138	3.8484	−0.0182	0.1903	163	Y_1
	0.1481	0.0156	4.6665	0.0289	0.1942	133	Y_2
	0.1474	0.0251	6.3616	0.0311	0.2164	204	Y_3
Casing axial	0.1611	0.1789	3.9954	−0.0008	0.4527	136	Y_1
	0.1618	0.2286	4.3712	−0.0331	0.5047	178	Y_1
	0.1603	0.4155	6.6553	−0.2794	0.6642	186	Y_3
Casing radial	0.1188	0.0273	3.3556	−0.0429	0.2035	161	Y_1
	0.1191	0.0424	3.3162	−0.0449	0.2383	162	Y_2
	0.1178	0.0777	3.4881	−0.0098	0.3027	177	Y_3

3.4. Cavitation Status Recognition

3.4.1. Motor Current Signal Recognition Results and Analysis

Figure 14 shows the results of the cavitation status recognition for the current signal under 1.0 Q_d by the BPNN. The overall accuracy of this recognition model is 76.8%. From the confusion matrices and ROC curves, it is evident that the classification performance for Y_3 is the best, while Y_1 and Y_2 exhibit some confusion, indicating that the model excels in recognizing severe cavitation but may make errors in distinguishing between non-cavitation and incipient cavitation. This is primarily attributed to the fact that, during incipient cavitation, the impact on the impeller is relatively weak, and cavitation features can be easily overshadowed by the power frequency signal, making it challenging to differentiate between non-cavitation and incipient cavitation. In contrast, severe cavitation in the current signal contains richer cavitation features, making them easier to extract and recognize.

Table 8 presents the results of the two recognition models of the BPNN and SVM. The BPNN outperforms the SVM in overall accuracy for all three operational conditions, exhibiting better recognition performance. However, both models have relatively lower recognition accuracy for Y_1 and Y_2. Additionally, the recognition accuracy of both models increases with higher flow rates, especially for Y_3, where the recognition accuracy is the highest at high flow rates; this is attributed to the fact that cavitation is more likely to occur at higher flow rates, resulting in a more significant number of bubbles and more intense cavitation collapse, which exerts a more substantial impact on the impeller. It aligns with the earlier observation that the variation in BIMF1-RMS is more pronounced under 1.25 Q_d conditions than other conditions. However, it also indicates that cavitation status recognition models based on current signals have lower sensitivity to cavitation under low-flow-rate conditions.

Table 8. Cavitation status recognition results of current signals.

Model	Flow Rate	Y_1	Y_2	Y_3	Accuracy	Overall Accuracy
BPNN	0.75 Q_d	50.3%	56.5%	92.6%	67.6%	73.9%
	1.0 Q_d	58.8%	64.3%	99.0%	76.8%	
	1.25 Q_d	63.1%	70.2%	99.4%	77.4%	
SVM	0.75 Q_d	47.1%	54.6%	91.4%	65.4%	71.0%
	1.0 Q_d	55.0%	65.9%	93.1%	72.4%	
	1.25 Q_d	60.0%	68.6%	94.3%	75.2%	

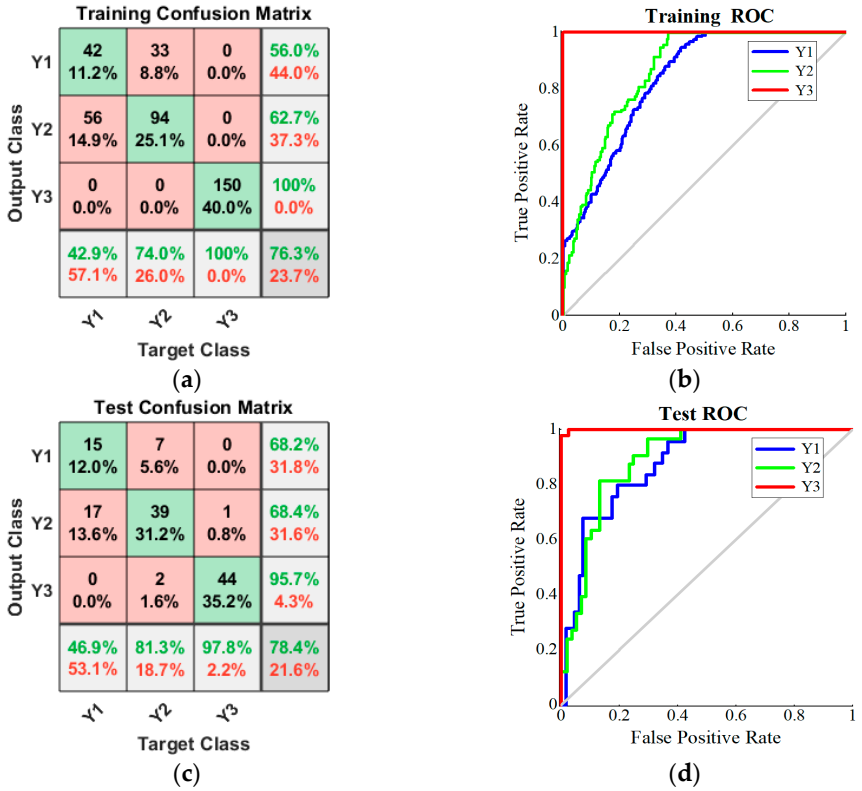

Figure 14. BPNN recognition results for motor current signals under 1.0 Q_d: (**a**) training confusion matrix; (**b**) training ROC; (**c**) test confusion matrix; (**d**) test ROC.

3.4.2. Vibration Signal Recognition Results and Analysis

The BPNN recognition results for different vibration measurement points at three operational conditions are presented in Table 9. The overall accuracy indicates that, except for the inlet, various vibration measurement points exhibit excellent recognition performance. Notably, compared to the current signal and other vibration measurement points, the casing axial measurement point exhibits higher BPNN recognition accuracy under all three operating conditions, effectively reflecting the impact of cavitation collapse on the axial direction of the impeller. Figure 15 illustrates the BPNN recognition results for the inlet measurement point under 1.0 Q_d conditions. The confusion matrices and ROC curves reveal that the recognition performance for the inlet measurement point is suboptimal, with errors in distinguishing between different cavitation statuses; this suggests that extracting meaningful cavitation features from the vibration signals at the inlet measurement point is challenging.

Table 9. BPNN cavitation status recognition results of different vibration measurement points.

Measurement Location	Flow Rate	Y_1	Y_2	Y_3	Accuracy	Overall Accuracy
Inlet	0.75 Q_d	63.5%	76.3%	49.7%	65.2%	67.4%
	1.0 Q_d	71.8%	80.2%	53.4%	70.4%	
	1.25 Q_d	65.1%	79.3%	49.3%	66.6%	
Outlet	0.75 Q_d	67.7%	64.5%	85.0%	78.0%	81.7%
	1.0 Q_d	76.3%	67.5%	89.3%	85.2%	
	1.25 Q_d	72.8%	66.7%	84.5%	81.8%	
Casing axial	0.75 Q_d	88.7%	85.7%	90.3%	88.6%	89.3%
	1.0 Q_d	89.9%	87.5%	91.4%	90.2%	
	1.25 Q_d	87.8%	86.9%	89.7%	89.2%	
Casing radial	0.75 Q_d	83.1%	89.3%	88.1%	83.6%	85.4%
	1.0 Q_d	84.8%	84.3%	88.9%	87.4%	
	1.25 Q_d	83.7%	86.7%	88.5%	85.2%	

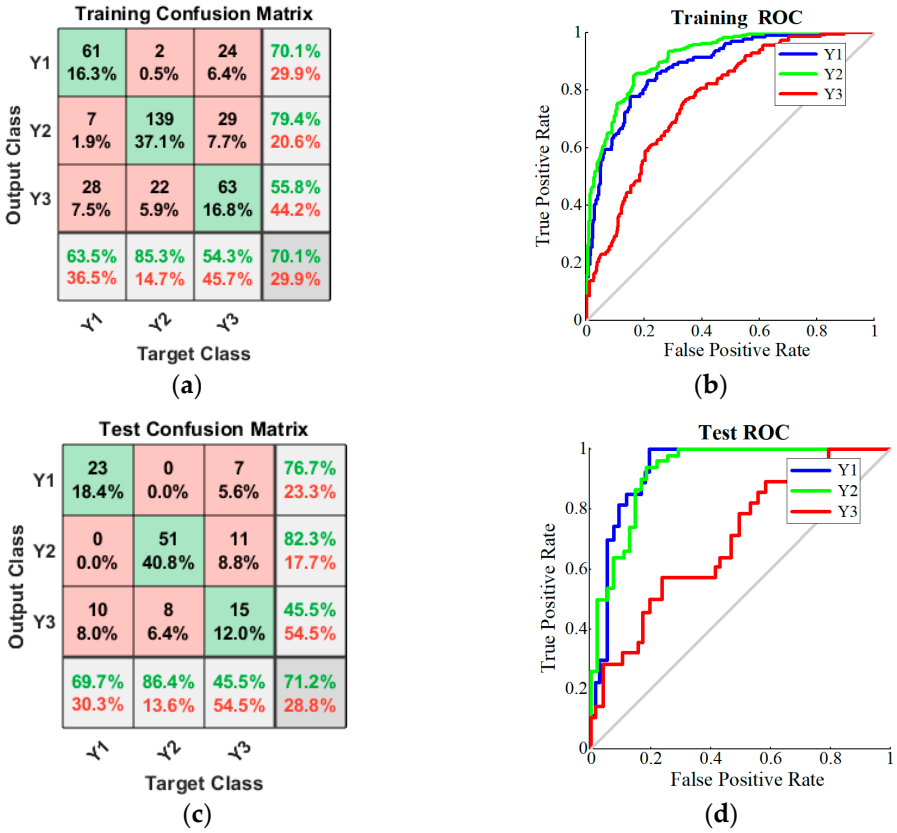

Figure 15. BPNN recognition results for inlet vibration measurement point at 1.0 Q_d: (**a**) training confusion matrix; (**b**) training ROC; (**c**) test confusion matrix; (**d**) test ROC.

The SVM recognition results for different vibration signals at three operational conditions are presented in Table 10. The casing axial and casing radial measurement points exhibit relatively high overall recognition accuracy, although the accuracy for the radial casing point decreases significantly under low-flow-rate conditions. In summary, the casing axial measurement point achieves consistently high cavitation state recognition accuracy across all operational conditions, similar to the results obtained with the BPNN; this underscores that the axial casing measurement point is the optimal vibration measurement location for cavitation monitoring in centrifugal pumps. Overall, the SVM cavitation recognition model based on vibration signals demonstrates slightly lower accuracy than the BPNN.

Table 10. SVM cavitation status recognition results of different vibration measurement points.

Measurement Location	Flow Rate	Y_1	Y_2	Y_3	Accuracy	Overall Accuracy
Inlet	0.75 Q_d	49.7%	48.4%	53.2%	63.0%	64.7%
	1.0 Q_d	51.9%	55.1%	65.3%	67.4%	
	1.25 Q_d	50.5%	57.2%	64.2%	63.6%	
Outlet	0.75 Q_d	78.9%	90.4%	83.3%	78.2%	78.1%
	1.0 Q_d	75.0%	79.5%	79.1%	79.2%	
	1.25 Q_d	79.6%	81.9%	82.4%	76.8%	
Casing axial	0.75 Q_d	86.7%	84.7%	88.3%	86.6%	87.0%
	1.0 Q_d	85.9%	83.5%	87.4%	88.2%	
	1.25 Q_d	83.8%	82.9%	89.7%	86.2%	
Casing radial	0.75 Q_d	75.1%	74.4%	76.0%	77.4%	82.6%
	1.0 Q_d	87.8%	85.3%	84.9%	86.4%	
	1.25 Q_d	82.7%	82.7%	85.5%	84.0%	

3.5. Feature-Level MSIF Recognition Results and Analysis

After standardizing the feature vectors of the current and vibration signals, a scatter plot is constructed with the RMS of the casing axial vibration signal as the X-axis and the BIMF1-RMS of the current signal as the Y-axis at 1.0 Q_d, as shown in Figure 16. It is evident that the non-cavitation status (Y_1) and the cavitation statuses (Y_2 and Y_3) can be distinctly separated, while there is some overlap between Y_2 and Y_3; this demonstrates the feasibility of feature-level information fusion between the current and vibration signals.

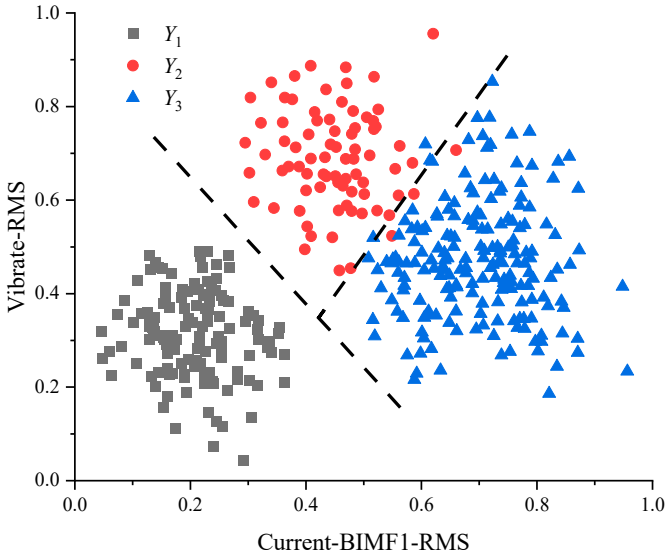

Figure 16. Scatter plot of casing axial vibration and current signals with feature-level fusion.

The recognition results of five types of feature-level information fusion based on the BPNN are shown in Table 11.

Table 11. Cavitation status recognition results based on feature-level information fusion with BPNN.

	Flow Rate	Y_1	Y_2	Y_3	Accuracy	Overall Accuracy
All vibration measurement points	0.75 Q_d	88.5%	87.6%	89.6%	96.4%	96.3%
	1.0 Q_d	94.6%	92.0%	91.5%	97.6%	
	1.25 Q_d	89.2%	89.2%	92.2%	95.0%	
Current Inlet	0.75 Q_d	53.6%	52.2%	57.3%	75.0%	71.5%
	1.0 Q_d	55.9%	59.4%	70.4%	76.8%	
	1.25 Q_d	54.4%	61.6%	69.2%	62.6%	
Current Outlet	0.75 Q_d	85.0%	97.4%	89.8%	86.4%	86.9%
	1.0 Q_d	80.8%	85.7%	85.2%	88.4%	
	1.25 Q_d	85.8%	88.3%	88.8%	85.8%	
Current Casing axial	0.75 Q_d	93.4%	91.3%	95.2%	96.4%	97.3%
	1.0 Q_d	92.6%	90.0%	94.2%	98.2%	
	1.25 Q_d	90.3%	89.3%	96.7%	97.2%	
Current Casing radial	0.75 Q_d	88.5%	87.6%	89.5%	91.0%	92.9%
	1.0 Q_d	94.6%	91.9%	91.5%	95.2%	
	1.25 Q_d	89.1%	89.1%	92.1%	92.6%	

The recognition results of five types of feature-level information fusion based on SVM are shown in Table 12.

Table 12. Cavitation status recognition results based on feature-level information fusion with SVM.

	Flow Rate	Y_1	Y_2	Y_3	Accuracy	Overall Accuracy
All vibration measurement points	0.75 Q_d	86.9%	86.0%	87.9%	95.2%	95.2%
	1.0 Q_d	92.9%	90.2%	89.8%	96.4%	
	1.25 Q_d	87.5%	87.5%	90.5%	94.0%	
Current Inlet	0.75 Q_d	52.1%	50.7%	55.7%	74.2%	70.7%
	1.0 Q_d	54.4%	57.7%	68.4%	75.8%	
	1.25 Q_d	52.9%	59.9%	67.3%	62.0%	
Current Outlet	0.75 Q_d	82.7%	94.7%	87.3%	85.4%	85.9%
	1.0 Q_d	78.6%	83.3%	82.9%	87.4%	
	1.25 Q_d	83.4%	85.8%	86.3%	84.8%	
Current Casing axial	0.75 Q_d	90.8%	88.7%	92.5%	95.4%	96.2%
	1.0 Q_d	90.0%	87.5%	91.6%	97.2%	
	1.25 Q_d	87.8%	86.8%	94.0%	96.0%	
Current Casing radial	0.75 Q_d	86.0%	85.2%	87.1%	90.0%	91.9%
	1.0 Q_d	92.0%	89.4%	88.9%	94.2%	
	1.25 Q_d	86.6%	86.6%	89.6%	91.6%	

Compared to the cavitation status recognition models based on a single sensor, as discussed earlier, whether using the BPNN or SVM, the recognition accuracy is significantly improved after information fusion. It indicates the feasibility of feature-level MSIF in centrifugal pump cavitation fault diagnosis, and it shows excellent applicability across different classification models. Tables 11 and 12 show that the information fusion of current and vibration signals effectively enhances cavitation recognition accuracy, particularly at low flow rates, overcoming the drawback of low cavitation sensitivity in current signals at low flow conditions. Moreover, it significantly improves the recognition accuracy of incipient cavitation. The vibration signals collected in this experiment have relatively high uncertainty and are susceptible to external environmental noise. In contrast, current signals are minimally affected by external factors. Therefore, the fusion of current and vibration signals enhances the model's resistance to interference and provides more reliable recognition results than vibration signals alone. While the fusion of multiple vibration measurement points also achieves similar effects, the fusion of current and a single vibration signal reduces the number of sensors required, making it more suitable for monitoring cavitation statuses in extreme conditions. Additionally, it reduces data acquisition costs, especially the fusion of current and the casing axial vibration measurement point, which yields the best recognition results.

4. Conclusions

This study employed non-intrusive sensors to collect motor current and vibration signals during cavitation in a centrifugal pump. Subsequently, it extracted and analyzed cavitation features from the signals and utilized a BPNN and SVM for cavitation status recognition. Furthermore, it employed feature-level MSIF to enhance the cavitation status recognition model's recognition accuracy and noise resistance. The main conclusions are as follows:

1. The flow rate significantly influences recognition accuracy, with lower flow rates resulting in lower recognition accuracy. It indicates the low sensitivity of the current signal to cavitation at low flow rates. Furthermore, it exhibits a weak discriminatory ability between non-cavitation and incipient cavitation, making it inadequate for practical engineering requirements.
2. The cavitation status recognition model based on vibration signals performs relatively well, especially with the highest recognition accuracy at the casing axial measurement point. However, the random uncertainty of the vibration signals obtained in this test was relatively high, indicating their limited reliability. Vibration signals may

not be suitable for engineering applications in extreme conditions with significant external noise. While combining multiple vibration measurement points can enhance recognition accuracy and resilience to interference, it also increases the cost associated with signal acquisition and computation.

3. The joint diagnosis of cavitation state based on the feature-level MSIF of current and vibration signals shows a significant improvement in recognition accuracy compared to a single sensor. Moreover, the accuracy distribution remains relatively stable and is less influenced by flow rates. Additionally, considering that current signals are less affected by external environmental noise, this approach enhances the system's resistance to interference. The coupling current and casing axial vibration monitoring scheme, using only two sensors, demonstrates the most noticeable improvement in cavitation status recognition accuracy, saving on signal acquisition and computation costs; it has great reference value for practical engineering applications.
4. The joint diagnosis of cavitation status using feature-level MSIF from current and vibration sensors under both the BPNN and SVM classification models significantly improves cavitation status recognition accuracy. It suggests that this method applies to different classification models.

This study utilized VMD to process the current signal, which effectively analyses and characterizes cavitation statuses in centrifugal pumps but lacks theoretical underpinnings. Future research could establish a detailed dynamic model of the impact of fluid on torque and current during cavitation in centrifugal pumps based on fluid dynamics, rotor dynamics, and electromagnetic coupling theories to better understand the dynamic relationship between centrifugal pump cavitation and current. The analysis of the reasons for the high random uncertainty in vibration signals lacked experimental confirmation. Furthermore, after filtering the vibration signals, only cavitation features in the time domain were extracted, which is relatively simple and provides limited cavitation information, restricting the accuracy of subsequent recognitions to some extent.

Author Contributions: Conceptualization, M.S., M.A. and X.W.; methodology, M.S. and Y.Z.; software, Y.Z.; validation, G.L., W.X. and X.W.; formal analysis, M.A.; resources, M.S.; data curation, M.S. and M.A.; writing—original draft preparation, M.S., M.A. and Y.Z.; writing—review and editing, G.L. and W.X.; supervision, G.L. and X.W. All authors have read and agreed to the published version of the manuscript.

Funding: The Shandong Province science and technology SMES innovation ability improvement project [2023TSGC0005]; the Technology Support Plan (Research on Key Industrial Technologies) [TG202251]; Key projects of the joint fund of the National Natural Science Foundation of China [U20A20292].

Data Availability Statement: Data available on request. The data underlying this article will be shared on request to the corresponding author.

Acknowledgments: Gratitude is extended to the Shandong Province science and technology SMES innovation ability improvement project for their financial support of this research. Special thanks to the China Nuclear Power Engineering Co., Ltd. (Beijing, China) and Wang Xiuli's research group at Jiangsu University for their technical assistance in this study.

Conflicts of Interest: Author Mengbin Song was employed by the company LEO Group Hunan Pump Co., Ltd. and Yifan Zhi was employed by the company China Nuclear Power Engineering Co., Ltd. The remaining authors declare that the research was conducted in the absence of any commercial or financial relationships that could be construed as a potential conflict of interest.

Nomenclature

n_s	Specific speed
Q_d	Rated flow rate (m^3/h)
Ψ	Cavitation number
P	Inlet static pressure (Pa)
E_S	Systematic uncertainty

f_m	Sensor uncertainty
k	Coverage factor
t_{n-1}	Confidence coefficient
K	Decomposition level
τ	Fidelity coefficient
e_i	Energy share
k_i	Kurtosis
η_i	RMS
T_1	Eigen-matrix of current signal
Y_1	Non-cavitation
Y_3	Severe cavitation
g	RBF self-contained function
H	Head (m)
n	Rotational speed (r/min)
σ	Head coefficient
P_v	Saturation vapor pressure (Pa)
E_r	Random uncertainty
f_c	System uncertainty of the acquisition instrument
S_x	Standard deviation
E	Comprehensive uncertainty
α	Penalty factor of VMD
ε	Convergence threshold
s_i	Variance
γ_i	Skewness
Q_t	Time-domain dimensionless characterization quantities
T_2	Eigen-matrix of vibration signal
Y_2	Incipient cavitation
C	Penalty factor of SVM
σ_{H}	Incipient cavitation number

References

1. Mousmoulis, G.; Karlsen-Davies, N.; Aggidis, G.; Anagnostopoulos, I.; Papantonis, D. Experimental analysis of cavitation in a centrifugal pump using acoustic emission, vibration measurements and flow visualization. *Eur. J. Mech. B Fluids* **2019**, *75*, 300–311. [CrossRef]
2. Lu, J.; Yuan, S.; Luo, Y.; Yuan, J.; Zhou, B.; Sun, H. Numerical and experimental investigation on the development of cavitation in a centrifugal pump. *Proc. Inst. Mech. Eng. Part E J. Process Mech. Eng.* **2016**, *230*, 171–182. [CrossRef]
3. Christopher, S.; Kumaraswamy, S. Identification of Critical Net Positive Suction Head from Noise and Vibration in a Radial Flow Pump for Different Leading Edge Profiles of the Vane. *J. Fluids Eng. Trans. Asme* **2013**, *135*, 121301. [CrossRef]
4. Pang, M.; Shu, L.; Lu, J.; Zhu, X.; Rodrigues, J. In A Case Study: Monitoring Heat Exchanger Based on Vibration Sensors and Nondestructive Testing Technique. In Proceedings of the 8th International ICST Conference on Communications and Networking in China (CHINACOM), Guilin, China, 14–16 August 2013; pp. 511–516.
5. Chudina, M. Noise as an indicator of cavitation in a centrifugal pump. *Acoust. Phys.* **2003**, *49*, 463–474. [CrossRef]
6. Sun, H.; Luo, Y.; Yuan, S.; Yin, J. Hilbert spectrum analysis of unsteady characteristics in centrifugal pump operation under cavitation status. *Ann. Nucl. Energy* **2018**, *114*, 607–615. [CrossRef]
7. Matloobi, S.M.; Riahi, M. Identification of cavitation in centrifugal pump by artificial immune network. *Proc. Inst. Mech. Eng. Part E J. Process Mech. Eng.* **2021**, *235*, 2271–2280. [CrossRef]
8. Azizi, R.; Hajnayeb, A.; Ghanbarzadeh, A.; Changizian, M. Cavitation Severity Detection in Centrifugal Pumps. In Proceedings of the 6th International Congress on Technical Diagnostics (ICTD), Gliwice, Poland, 12–16 September 2018; pp. 47–55.
9. Sun, H.; Yuan, S.; Luo, Y. Cyclic Spectral Analysis of Vibration Signals for Centrifugal Pump Fault Characterization. *IEEE Sens. J.* **2018**, *18*, 2925–2933. [CrossRef]
10. Zhang, Y.; Dong, L.; Song, L. Sensitivity of vibration measuring point location to cavitation of centrifugal pump. *J. Vib. Shock.* **2022**, *41*, 90–97.
11. Kong, S.; Li, J.; Yang, M.; Chen, J. The Noise Test System and Solution Measures of Vibration Test. In Proceedings of the International Conference on Manufacturing Engineering and Automation (ICMEA), Guangzhou, China, 16–18 November 2012; pp. 1925–1926.
12. Kipervasser, M.V.; Gerasimuk, A.V.; Simakov, V.P. Development of the pump protection system against cavitation on the basis of the stator current signature analysis of drive electric motor. In Proceedings of the 11th All-Russian Scientific and Practical Conference (with International Participation) on Automation Systems in Education, Science and Production, Novokuznetsk, Russia, 14–16 December 2018.

13. Sunal, C.E.; Dyo, V.; Velisavljevic, V. Review of Machine Learning Based Fault Detection for Centrifugal Pump Induction Motors. *IEEE Access* **2022**, *10*, 71344–71355. [CrossRef]
14. Sun, H.; Yuan, S.; Luo, Y. Characterization of cavitation and seal damage during pump operation by vibration and motor current signal spectra. *Proc. Inst. Mech. Eng. Part A J. Power Energy* **2019**, *233*, 132–147. [CrossRef]
15. Liang, X.; Luo, Y.; Deng, F.; Li, Y. Application of Improved MFDFA and D-S Evidence Theory in Fault Diagnosis. *Appl. Sci.* **2022**, *12*, 4976. [CrossRef]
16. Liu, X.; Chong, X.; Zhen, C. Application of the Technology of Multi-source Information Fusion in Industrial Monitoring and Fault Diagnosis. In Proceedings of the 2nd International Conference on Energy and Environmental Protection (ICEEP 2013), Guilin, China, 19–21 April 2013; pp. 3088–3089.
17. Dong, L.; Zhu, J.C.; Wu, K.; Dai, C.; Liu, H.L.; Zhang, L.X.; Guo, J.N.; Lin, H.B. Cavitation Status Recognition Method of Centrifugal Pump Based on Multi-Pointand Multi-Resolution Analysis. *J. Appl. Fluid Mech.* **2021**, *14*, 315–329.
18. Wang, H.; Li, S.; Song, L.; Cui, L. A novel convolutional neural network based fault recognition method via image fusion of multi-vibration-signals. *Comput. Ind.* **2019**, *105*, 182–190. [CrossRef]
19. Gong, B.; Yuan, S.; Luo, Y.; Han, Y.; Dong, J. Vibration signal characteristics of centrifugal pumps with cavitation erosion impellers. *J. Vib. Shock.* **2020**, *39*, 92–99.
20. Chen, Y.; Zhang, P. Bearing Fault Detection Based on SVD And EMD. In Proceedings of the International Conference on Frontiers of Mechanical Engineering and Materials Engineering (MEME), Hong Kong, China, 27–29 July 2012; pp. 70–74.
21. Dou, C. Fault Feature Extraction for Gearboxes Using Empirical Mode Decomposition. In Proceedings of the International Conference on Manufacturing Science and Technology (ICMST), Singapore, 16–18 September 2012; pp. 1376–1380.
22. Yue, Y.; Sun, G.; Cai, Y.; Chen, R.; Wang, X.; Zhang, S. Comparison of performances of variational mode decomposition and empirical mode decomposition. In Proceedings of the 3rd International Conference on Energy Science and Applied Technology (ESAT), Wuhan, China, 25–26 June 2016; pp. 469–476.
23. Dragomiretskiy, K.; Zosso, D. Variational Mode Decomposition. *IEEE Trans. Signal Process.* **2014**, *62*, 531–544. [CrossRef]
24. Su, N.; Li, X.; Zhang, Q. Fault Diagnosis of Rotating Machinery Based on Wavelet Domain Denoising and Metric Distance. *IEEE Access* **2019**, *7*, 73262–73270. [CrossRef]
25. Rajeswaran, N.; Madhu, T.; Kalavathi, M.S. Fault Diagnosis and Testing of induction machine using Back Propagation Neural Network. In Proceedings of the IEEE International Power Modulator and High Voltage Conference (IPMHVC), San Diego, CA, USA, 3–7 June 2012; pp. 492–495.
26. Widodo, A.; Yang, B.-S. Support vector machine in machine condition monitoring and fault diagnosis. *Mech. Syst. Signal Process.* **2007**, *21*, 2560–2574. [CrossRef]
27. Qi, X.; Wu, X.; Ji, Y.; Wang, X.; Li, H. Research on Classification of Power Load Data Based on LIBSVM. In Proceedings of the 11th International Conference on Intelligent Human-Machine Systems and Cybernetics (IHMSC), Hangzhou, China, 24–25 August 2019; pp. 158–162.
28. Qin, B.; Liu, B. Prediction of Sewage Wastewater Quality Based on PSO-LIBSVM. In Proceedings of the International Symposium on Computers and Informatics (ISCI), Beijing, China, 17–18 January 2015; pp. 280–286.
29. Xie, Y.; Zhang, J. Research on the Fault Diagnosis Method for Hoisting Machinery Based on Multi-source Information Fusion and BPNN. In Proceedings of the International Conference on Artificial Intelligence—Technologies and Applications (ICAITA), Bangkok, Thailand, 24–25 January 2016.
30. Wang, Z.; He, X.; Shen, H.; Fan, S.; Zeng, Y. Multi-source information fusion to identify water supply pipe leakage based on SVM and VMD. *Inf. Process. Manag.* **2022**, *59*, 102819. [CrossRef]
31. Li, Y.; Zhao, M.; Xu, M.; Liu, Y.; Qian, Y. Analysis and Comparison of Multi-Source Information Fusion Technologies. In Proceedings of the 5th International Conference on Fuzzy Systems and Data Mining (FSDM), Kitakyushu, Japan, 18–21 October 2019; pp. 1057–1063.